Energy Engineering

Tech Science Press

Doi:10.32604/ee.2026.076354

ARTICLE

Fault Location of Distribution Network Based on Traveling Wave Head Inversion

Guanghua He[1], Jinlong Qi[1,*], Yao Feng[1], Jiayi Han[1], Heng Chen[2], Baoming Huang[3] and Jiangtao Li[3]

[1]Wuxi Power Supply Company, State Grid Jiangsu Electric Power Company, Wuxi, 214000, China
[2]Shandong Kehui Electric Automation Co., Ltd., Zibo, 255000, China
[3]School of Electrical Engineering, Xi'an Jiaotong University, Xi'an, 710049, China

*Corresponding Author: Jinlong Qi. Email: qjl1993_wx@163.com

Received: 19 November 2025; Accepted: 26 December 2025; Published: 27 May 2026

ABSTRACT: The identification of the traveling wave head is an important factor affecting the accuracy of fault traveling wave positioning. In practice, in addition to the attenuation of traveling wave amplitude and rising speed caused by distribution line factors, various traveling wave sensors can also cause transmission distortion of high-frequency traveling wave signals, which in turn affects the calibration of traveling wave arrival time and the accuracy of fault distance measurement. The inversion technology of sensor transmission characteristics using analytical methods has limited ability to reflect factors such as stray capacitance and sensor differences. In comparison, data-driven artificial intelligence modeling inversion technology can better capture the details of sensor transmission characteristics and help improve positioning accuracy. Regarding this issue, a fault location method for distribution lines based on initial traveling wave head inversion is proposed in this paper. Firstly, the mechanism of fault traveling wave propagation distortion, including distribution lines and sensor factors, was analyzed. Furthermore, a traveling wave head inversion method based on a one-dimensional convolutional neural network was proposed. This method constructs an inversion model by training the detail coefficients of the primary and secondary traveling wave heads of the sensor after the wavelet transform as samples. Based on the training model, the wavelet detail coefficients of the secondary side wave after the fault occurs are inverted into the corresponding primary side coefficients, and the arrival time of the wave head is accurately extracted through the wavelet modulus maximum method, thereby improving the positioning accuracy of the double-ended traveling wave method. Experiments show that the average location error of this method does not exceed 2.2% under various fault conditions with a sampling rate of 1 MHz, and demonstrating the robustness and reliability of this method in complex fault scenarios.

KEYWORDS: Traveling wave fault location; inversion of traveling wave head; convolutional neural network; voltage sensor; wavelet transform

1 Introduction

The rapid and accurate positioning of fault points is of great significance in reducing repair time and improving power supply reliability. Among numerous fault location techniques, the positioning technology of traveling wave, which is achieved by capturing the arrival time difference or reflected wave characteristics of transient traveling waves, has been widely applied in the field of power transmission [1]. With the continuous expansion of the distribution network scale and the widespread access to distributed power sources, power companies have continuously raised their requirements for the reliability of the distribution network power supply, and the traveling wave positioning technology for distribution networks has gradually attracted the attention of industry researchers [2,3].

Traveling wave positioning is mainly divided into two types: single-ended and double-ended methods. The single-ended method requires the identification of reflected waves from the fault point, due to the numerous branch lines in the distribution network, it is difficult to identify reflected waves, resulting in a gap between the single ended method and practical applications [4,5]. The double-ended method only requires identification of the initial wave head, without the need to identify the refracted and reflected waveforms, and has high reliability. Therefore, the fault location of the distribution network based on the double-ended method has become the most practical method for fault location [6]. The basic principle of the traveling wave method for fault location is to capture the arrival time difference or reflected wave characteristics of transient traveling waves to achieve fault location. Due to the influence of line losses and traveling wave dispersion during transmission, the amplitude and rise rate of the fault traveling wave head will be attenuated and distorted. Therefore, analyzing the traveling wave head to identify the arrival time of the initial traveling wave is one of the key technologies for traveling wave location [7,8]. Reference [9] proposed a wide area network fault location technology based on traveling wave technology, which uses discrete wavelet transform to identify the arrival time of the traveling wave head. Reference [10] proposed a fault location method for multi-terminal transmission line based on the time–frequency analysis of fault traveling wave. Aiming at the problem of waveform distortion of the secondary traveling wave obtained from the primary traveling wave signal transmitted by the voltage traveling wave sensor, an accurate detection method of voltage traveling wave based on ensemble empirical mode decomposition and L1 norm least squares regularization is proposed [11]. Aiming at the calculation of traveling wave velocity and the calibration of traveling wave head, the mapping relationship between the frequency of wave head and fault distance/fault pole is constructed in reference [12], where a neural network model suitable for fault location and fault pole identification is designed. Reference [13] proposed a fault signal filtering algorithm based on the improved empirical mode decomposition and Fast Fourier Transform, and an inversion model of incident waves was constructed based on this algorithm to improve positioning accuracy.

Compared to transmission lines, the attenuation and distortion of the traveling wave head in distribution lines are more complex due to the presence of more mixed lines in the distribution network and the severe attenuation of zero mode components caused by the absence of lightning protection wires in overhead lines [14,15], the traditional transmission line technology that only utilizes current traveling waves cannot meet the requirements of fault location for distribution lines [16]. Moreover, due to the significant wave impedance difference between cables and overhead lines, using only current traveling waves for fault location has significant limitations in terms of traveling wave detection sensitivity and engineering implementation [17]. Therefore, the mixed use of multiple types of traveling wave sensors is also one of the characteristics of traveling wave fault location technology in distribution networks [18–20]. Reference [21] proposed a fault traveling wave head calibration method based on an improved optical voltage sensor. Reference [22] utilized the relationship between the primary and secondary signals of a voltage sensor, derives a waveform inversion model using the deconvolution principle, and combines it with the stochastic resonance algorithm to realize positioning utilizing voltage traveling waves. Reference [23] utilized a novel hybrid fiber optic sensor to obtain wideband transient traveling waves and achieve dual-ended method traveling wave location in a predetermined interval. Reference [24] designed a voltage sensor using devices such as resistors, inductors, and capacitors, and connected it to the power grid via capacitors for the conversion of voltage and current traveling wave signals. Reference [25] proposed a multi-scale waveform inversion method regarding the nonlinear transmission characteristics of traveling wave sensors and the ill-posed problems in the inversion process, to achieve high-precision and accurate measurement of power grid fault traveling wave signals. Reference [26] designed an online calibration system for electronic voltage sensors, using an improved Rife frequency shift algorithm for signal processing to complete data calibration without causing interference to

the power grid, thereby improving the accuracy of sensor measurement. Reference [27] designed a voltage current combination sensor, which is based on the electric and magnetic field strength near the three-phase overhead line. By reverse solving the measured electric and magnetic field values, non-contact measurement of voltage and current is achieved. Reference [28] utilized inductive coupling capacitors to capture transient current signals, achieving non-invasive cable fault diagnosis. Reference [29] conducted research on the TMR current sensor method and response situation, and developed an intelligent TMR sensor device for precise measurement of wide area signals in distribution networks, which can locate the arrival time of the wave head of current traveling wave accurately. Overall, the research on current traveling wave sensors represented by Roche coils is relatively mature [30]. In contrast, although there are also some studies on traveling wave voltage sensors, the calibration method and even the arrival time of the traveling wave head for eliminating distortion effects caused by transmission characteristics of such sensors are less concerned.

On the whole, in addition to the attenuation of traveling waves caused by distribution line, various traveling wave sensors can also cause transmission distortion of high-frequency traveling wave signals, which in turn affects the calibration of traveling wave arrival time and the accuracy of fault distance measurement. The inversion technology of sensor transmission characteristics using analytical methods has limited ability to reflect factors such as stray capacitance and sensor differences. Artificial intelligence technology provides a new way to solve this problem, and data-driven technologies such as Convolutional Neural Network (CNN) has significant advantages in model detail description due to their ability to automatically extract local features of input data [31,32]. With the aim of accurately inverting the fault traveling wave head of the sensor on the primary side and improving the calibration accuracy of the arrival time of the wave head, this paper proposes a traveling wave head inversion method based on a CNN which can better capture the details of sensor transmission characteristics and help improve positioning accuracy. The paper focuses on the application scenario of Capacitive Voltage Transformer (CVT) sensors used for cable traveling wave monitoring, by inverting the wavelet detail coefficients of the primary voltage traveling wave, the arrival time calibration correction of the initial traveling wave head is achieved, and the effectiveness of this method is verified by combining it with the double-ended positioning method, aiming to provide new ideas and references for traveling wave positioning technology.

2 Principle of Traveling Wave Attenuation

During the propagation of fault traveling waves, the wave head will be distorted due to the influence of line parameters firstly. Secondly, in the process of obtaining traveling waves using sensors, the transmission characteristics of sensors will further deepen the degree of traveling wave distortion, which will seriously affect the identification accuracy of the arrival time of the wave head.

2.1 Traveling Wave Attenuation Caused by the Line

Transient traveling waves caused by faults transmitted in cables and overhead lines may experience attenuation distortion caused by line parameters. According to the transmission line theory, the time-frequency forms of voltage and current can be obtained, as shown in Eqs. (1) and (2):

$$\begin{aligned} u_x(x,t) &= \sqrt{2}\,|\mathrm{A}_1|\, e^{-\alpha x}\cos(\omega t-\beta x+\varphi_1) \\ &\quad+\sqrt{2}\,|\mathrm{A}_2|\, e^{-\alpha x}\cos(\omega t+\beta x+\varphi_2) \end{aligned} \tag{1}$$

$$\begin{aligned} i_x(x,t) &= \sqrt{2}\frac{|\mathrm{A}_1|}{Z_0}e^{-\alpha x}\cos(\omega t-\beta x+\varphi_1) \\ &\quad+\sqrt{2}\frac{|\mathrm{A}_2|}{Z_0}e^{-\alpha x}\cos(\omega t+\beta x+\varphi_2) \end{aligned} \tag{2}$$

where A_1 and A_2 are constants, α is the attenuation constant, and β is the phase constant. From the above two formulas, it can be inferred that the waveform of the fault traveling wave is not only related to time t, but also to the transmission distance x.

Fig. 1 shows the shape of the voltage traveling wave head at the monitoring point under different transmission distances. It can be known that as the transmission distance increases, the distortion of the traveling wave head becomes more pronounced: the amplitude of the wave head gradually decreases, the steepness of the waveform gradually becomes smoother, and the time delay of the wave head increases.

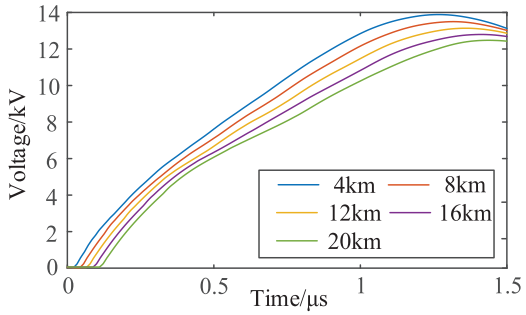

Figure 1: Comparison of voltage traveling wave head waveforms under various transmission distances at monitoring point

The above phenomenon is analyzed as follows:

(1) During the propagation of traveling waves, line resistance and insulation leakage conductivity can lead to attenuation of the amplitude of the traveling wave, and this loss effect becomes more significant as the length of the line increases.

(2) Affected by the skin effect, the high-frequency components of traveling waves suffer from severe energy loss during transmission, resulting in an accelerated amplitude attenuation rate of the high-frequency components. The higher the frequency of the components, the more significant the impact, ultimately leading to a reduction in the steepness of the traveling wave head.

2.2 Traveling Wave Distortions Caused by the Sensor

When the fault traveling wave reaches the monitoring points at both ends of the line after propagation through the line, the voltage sensor senses changes in the electromagnetic field and generates the secondary signal. Since traditional voltage sensors based on electromagnetic induction principles cannot be used for traveling wave sensing due to their narrow frequency band, we analyze the CVT used for cable voltage traveling wave sensing.

As shown in Fig. 2, CVT mainly includes metal plates, voltage divider capacitors, intermediate sensors, compensating reactors, shielding covers, and other structures. By wrapping the cable with metal plates and fixing it with specialized fixtures, the voltage divider capacitors and related electromagnetic units are used to output the secondary voltage.

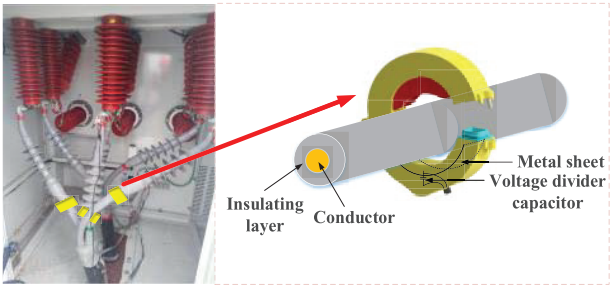

Figure 2: Schematic diagram of CVT

Due to the electric field effect, an equivalent capacitance exists between two insulated conductors. For CVT, stray capacitance does not affect the waveform during low-frequency operation, for the high-frequency stage, the stray capacitance cannot be ignored. Considering the internal structure of CVT, its stray capacitance is mainly distributed between the compensating reactor voltage, the primary winding to ground voltage of the sensor, the secondary winding to ground voltage of the sensor, and the primary winding to secondary winding voltage of the sensor. Based on this, an equivalent circuit model of CVT with stray capacitance was established in Fig. 3.

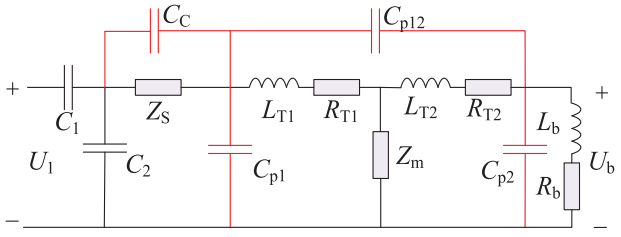

Figure 3: Equivalent circuit model for CVT with stray capacitance

In Fig. 3, U_1 represents the input voltage on the primary side, U_b represents the secondary voltage, C_1 and C_2 represent high voltage and medium voltage capacitors, respectively, Z_s represents the equivalent impedance of the compensating reactor, C_c represents the stray capacitance of the compensating reactor, Z_m represents the excitation impedance of the intermediate sensor T, R_{T1} and L_{T1} respectively represent the winding resistance and winding leakage inductance on the primary side of the intermediate sensor, R_{T2} and L_{T2} represent the winding resistance and winding leakage inductance on the secondary side of the intermediate sensor, respectively, C_{p1} represents the stray capacitance of the primary winding of the intermediate sensor to ground, C_{p2} represents the stray capacitance of the secondary winding of the intermediate sensor to ground, C_{p12} represents the coupling capacitance between the primary and secondary windings of the intermediate sensor, R_b and L_b are the equivalent resistance and inductance converted from the load to the primary side.

According to Fig. 3, the transfer function of CVT can be expressed in Eq. (3):

$$\begin{cases} H(s) = \dfrac{U_b(s)}{U_1(s)} = \dfrac{K_1}{K_2} \\ K_1 = (Z_2//Z_5)\,//\,(Z_3//Z_4) + (Z_6//Z_7//Z_8) \\ K_2 = \left(\dfrac{1}{sC} + Z_1\right) + (Z_2//Z_5)\,//K_3 \\ K_3 = [(Z_3//Z_4) + (Z_6//Z_7//Z_8)] \end{cases} \tag{3}$$

where:

$$\begin{cases} C = C_1 + C_2; \\ Z_1 = Z_s // [1/(sC_c)]; \\ Z_2 = 1/(sC_{p1}); \\ Z_3 = 1/(sC_{p12}); \\ Z_4 = (R_{T1} + sL_{T1}) + (R_{T2} + sL_{T2}) \\ + (R_{T1} + sL_{T1})(R_{T2} + sL_{T2})/Z_m; \\ Z_5 = (R_{T1} + sL_{T1}) + Z_m \\ + (R_{T1} + sL_{T1}) Z_m/(R_{T2} + sL_{T2}); \\ Z_6 = (R_{T2} + sL_{T2}) + Z_m \\ + (R_{T2} + sL_{T2}) Z_m/(R_{T1} + sL_{T1}); \\ Z_7 = 1/(sC_{p2}); Z_8 = R_b + sL_b \end{cases} \tag{4}$$

The stray capacitance can be calculated by Eq. (5):

$$C_x = \frac{4(n-1)\varepsilon_r \varepsilon_0 LDN}{3n^2 d} \tag{5}$$

where C_x is the stray capacitance, N is the number of turns in the coil, n is the number of layers in the coil, L is the average turn length, d is the distance between winding layers, D is the cross-sectional diameter of the wire, ε_r is the relative dielectric constant, and ε_0 is the vacuum dielectric constant.

Due to the low-pass characteristic of the transfer function of the sensor, high-frequency components in traveling waves are suppressed. According to Eq. (4), it can be seen that Z_1, Z_2, Z_3, and Z_7 are most sensitive to changes in signal frequency, especially for high-frequency traveling wave signals. Under high-frequency signals, its value is almost zero, where Z_2 and Z_7 serve as the capacitive reactance of the sensor to ground, providing a capacitive leakage path for high-frequency components to ground, resulting in the suppression and severe attenuation of high-frequency components in the secondary side wave head of the sensor. Fig. 4 shows the comparison of the wave head of the voltage traveling between the primary and secondary sides of the sensor. It can be seen that after the transformation caused by the sensor, the wave head of the secondary side slows down noticeably, the peak value decreases, and the peak value corresponds to a time lag compared to the wave head of the primary side.

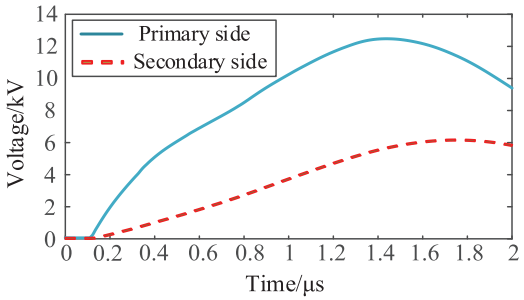

Figure 4: Comparison of the voltage traveling wave head between the primary and secondary sides of CVT

The accuracy of fault location depends on the calibration of the arrival time of the traveling wave head. Based on the analysis in Sections 2.1 and 2.2, the traveling wave head is inevitably affected by the line and

sensor during transmission, resulting in attenuation and distortion, which may cause a significant deviation in the time difference between the arrival of the traveling wave at both ends of the line compared to the actual situation. If the calibration time of the measured secondary traveling wave head is directly used, it will cause significant errors in the distance measurement of the two end traveling waves. Therefore, based on the transmission characteristics of the sensor, it is proposed to invert and reconstruct the primary side traveling wave head by inverting the secondary side traveling wave head.

However, by analyzing the equivalent circuit of the CVT shown in Fig. 3, it was found that in the actual production process, due to factors such as the manufacturer's manufacturing process, there may be some deviation between the stray capacitance parameter values calculated between the formula parameter and the actual parameter values, resulting in significant errors in the calculated CVT transmission characteristics compared to the actual situation. In addition, the calculation of stray capacitance mainly relies on the information of resonance points in the transmission characteristics of CVT voltage amplitude, which is a complex and computationally intensive method. Furthermore, it can be seen from Eqs. (4) and (5) that the transfer function of CVT not only has a complex structure, but also involves numerous parameters in each part. Once calculated incorrectly, it is likely to result in the CVT transmission characteristics obtained being vastly different from the actual situation.

Therefore, a simple and reliable method is needed to obtain the inverse transmission characteristics of CVT and improve the accuracy of the calibration time of the traveling wave head.

3 Wave Head Correction Method Based on CNN

Compared to traditional methods such as manual computation, neural networks do not require a detailed understanding of the internal structure and related parameters of sensors. They can be trained using only relevant samples and obtain mapping relationships that meet the requirements. This not only improves accuracy but also saves labor costs. Therefore, a neural network method is used to obtain the transmission characteristics of the sensor.

3.1 Feature Extraction Method

This paper chooses the wavelet transform as the tool for feature extraction, mainly relying on its excellent time-frequency localization analysis ability. Compared with the Fourier transform, the wavelet transform is more capable of analyzing the local characteristics of signals at different scales and times, especially for characterizing transient changes in signals when faults occur. The formula of the Discrete Wavelet Transform (DWT) is shown in Eq. (6):

$$WT_f(m,n) = \int_R f(t) \bullet \overline{\psi_{m,n}(t)} dt \tag{6}$$

where $WT_f(m, n)$ represents the coefficients obtained by the DWT, m and n represent scale and displacement parameters, $f(t)$ represents the original signal, $\psi_{m,n}(t)$ represents the wavelet basis function, and $\psi_{m,n}(t) = 2^{-m/2}\psi(2^{-m}t - n)$.

As shown in Fig. 5, the signal diagrams of each level are decomposed using db4, db6, and db8 wavelet bases, respectively. Compared to the db4 wavelet, the db6 has a longer support length and smoother waveform, which can more accurately capture the high-frequency transient components of fault traveling waves, and compared with db8 wavelet, db6 achieves a better balance between computational complexity and feature sensitivity, avoiding the loss of details in the wave head caused by excessive smoothing, and also avoiding the risk of overfitting. Thus, the db6 wavelet basis was ultimately selected.

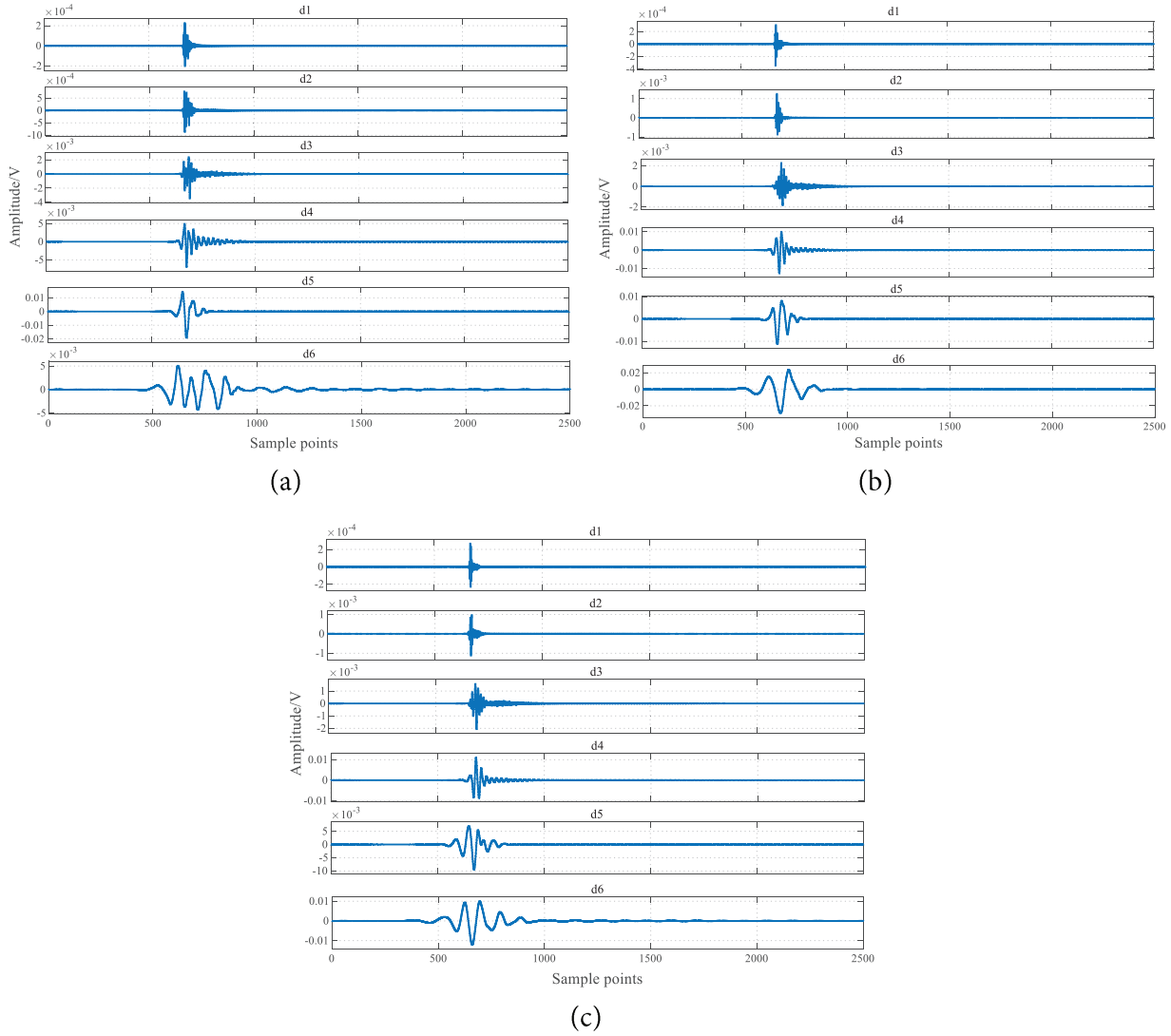

Figure 5: Signals from different decomposition levels of db4, db6, and db8 wavelets: (**a**) db4; (**b**) db6; (**c**) db8

After selecting the db6 wavelet basis for decomposition, in order to determine the arrival time of the wave head accurately, energy needs to be highly concentrated in a shorter time interval. For this purpose, it is necessary to evaluate the degree of energy concentration of detail coefficients at various scales. Firstly, use Eq. (7) to calculate the total energy of the detail coefficients for each layer:

$$E_j = \sum_{k=1}^{N_j} \left(d_j(k) \right)^2 \tag{7}$$

where E_j represents the total energy of each layer's detail coefficient, $d_j(k)$ represents the kth value of the jth layer's detail coefficient, and N_j represents the sample of the jth layer's coefficient.

After calculating the total energy of the detail coefficients in each layer, it is necessary to analyze the data interval where the energy concentration of each layer is located and determine the length of the interval (measured in L data points). The calculation method for energy concentration is as follows:

$$\mathrm{ECD} = \frac{E_L}{E_j} \tag{8}$$

Adjust L to achieve maximum ECD. The smaller the corresponding L value, the higher the energy concentration. Table 1 shows the L values and corresponding ECD values of each decomposition layer ($d1$~$d6$) calculated based on the db6 wavelet basis.

Table 1: Relationship between different layers of wavelet coefficient and interval length and energy

Number of layers	*d*1	*d*2	*d*3	*d*4	*d*5	*d*6
L	88	124	472	402	332	556
ECD	Highest	Higher	Low	Low	Low	Lowest

The results show that the energy concentration of the first layer decomposition is the highest, which can maximize the preservation of high-frequency details and steep features of the initial traveling wave head.

3.2 Convolutional Neural Network

Convolutional Neural Networks has the advantage of achieving local perception, effectively capturing local features of signals, and extracting more details. Moreover, since the convolutional layers in CNN utilize convolutional kernels for weight sharing, which can significantly reduce network parameters and effectively prevent overfitting problems that may exist in other neural networks during training. Furthermore, the pooling layer can also reduce the dimensionality of network parameters, accelerate training speed, and improve the generalization ability. Due to the parallel computation of convolution and pooling operations in CNN, the training efficiency is further improved. Thus, the CNN architecture is selected in this paper, which use the amplitude characteristics of the traveling waves on the primary and secondary sides of the sensor at different times as training samples to obtain the inverse transfer characteristics of the sensor.

The structure of CNN is shown in Fig. 6, which generally consists of an input layer, a convolutional layer, a pooling layer, a fully connected layer, and an output layer.

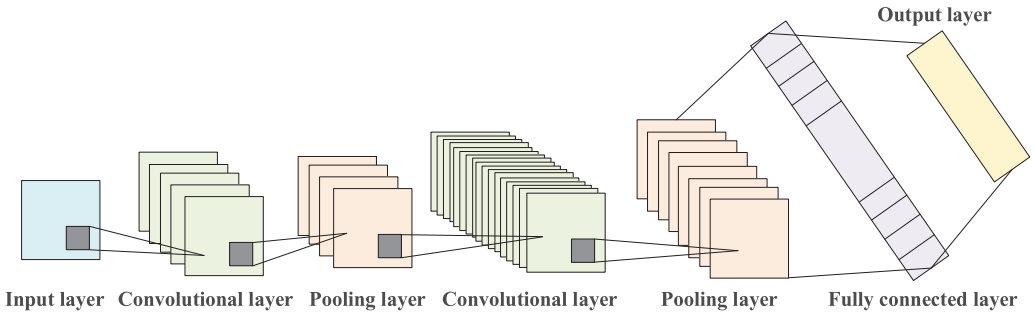

Figure 6: Architecture diagram of CNN

The most important part of CNN is the convolutional layer, which convolves the feature map of the previous layer with the convolutional kernel, and then passes the activation function to obtain a new feature map that is passed on to the next layer, represented by Eq. (9):

$$y_i = f\left(y_{i-1} \otimes W_i + b_i\right) \tag{9}$$

where $f(x)$ is the activation function, y_i represents the feature map of the i-th layer, W_i represents the weight matrix of the i-th convolutional kernel, the operation symbol "⊗" represents the convolution operation, and b_i is the bias vector of the i-th layer.

The pooling layer selects the features extracted from the previous convolutional layer, which not only reduces the dimensionality of network parameters to improve training efficiency, but also effectively alleviates the problem of model overfitting, as represented by Eq. (10), where p represents the pooling operation.

$$y_i = p\left(y_{i-1}\right) \tag{10}$$

The fully connected layer is composed of two adjacent layers of neurons connected to each other, usually located at the end of the CNN structure. Its input is a one-dimensional vector formed by tiling high-dimensional features extracted by convolutional and pooling layers, and bias is added to each neuron. Finally, the output feature map is obtained through an activation function, which can be represented as:

$$y_i = f\left(y_{i-1} \cdot W_i + b_i\right) \tag{11}$$

For multi-classification problems, Softmax is commonly used as the output layer to establish a mapping relationship between the input signal and the label, thereby achieving classification of the input signal. The function expression is shown in Eq. (12).

$$\text{Soft}\max(x)_i = \frac{e^{x_i}}{\sum_{j=1}^{k} e^{x_j}} \tag{12}$$

where x_i represents the i-th output variable of the Softmax layer, k represents the number of neurons in the input Softmax layer, Softmax $(x)_i$ represents the probability of the i-th output variable corresponding to the category within the range of $[0, 1]$. Therefore, after Softmax processing, the probability of each output variable belonging to each category can be obtained, and the results of multiple classifications can be presented in probability form.

Thus, a dataset is constructed by extracting features from the original voltage traveling wave signals on the primary and secondary sides of the sensor, which serve as the training samples for the neural network. Each training sample is defined as an input-output pair: the input array represents the $d1$ layer detail coefficient sequence obtained by wavelet decomposition of the secondary side voltage traveling wave of the sensor within a specified time window, which characterizes the high-frequency characteristics of the signal transmitted through the sensor. The output array is the $d1$ layer detail coefficient sequence extracted from the wavelet decomposition of the primary side voltage traveling wave of the sensor that is strictly aligned in time, representing the high-frequency characteristics of the original undistorted traveling wave.

By training the nonlinear mapping relationship of CNN, the distortion characteristics introduced by the sensor during the transmission of traveling wave signals can be captured. When a fault actually occurs, the neural network is used to invert the $d1$ layer detail coefficients of the primary side, avoiding nonlinear distortion of the sensor. By suppressing the high-frequency feature distortion caused by transmission

distortion, the high-frequency detail coefficients output by the model can more accurately reflect the time information of the original traveling wave reaching the inflection point, thereby improving the accuracy of the wave head arrival time calibration.

3.3 Dual Ended Traveling Wave Fault Location Method

The principle of fault location using the double-ended traveling wave method is shown in Fig. 7. L represents the total length of the line, the distance between the fault point and the M end is x, and the propagation speed of the traveling wave is v. The calculation of fault distance is as follows:

$$x = \frac{L + v \cdot (t_M - t_N)}{2} \tag{13}$$

where t_M represents the time it takes for the traveling wave to travel from the fault point to the M end, and t_N represents the transmission time from the fault point to the N end.

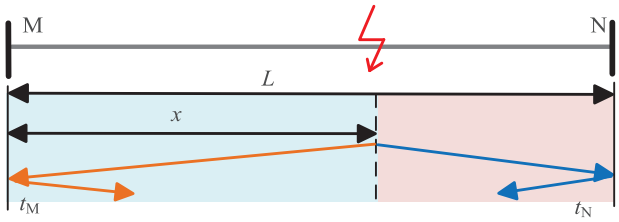

Figure 7: Schematic of double-ended traveling wave fault location

The calibration accuracy of t_M and t_N determines the positioning accuracy of the fault traveling wave. Among various calibration methods, due to the excellent time-frequency analysis ability of wavelet transform technology, this paper uses a traveling wave head calibration method based on wavelet modulus maximum, whose formula is as follows:

$$T_{d\max} = \mathrm{t}\left[\max\left(\left|d_{j,k}\right|\right)\right] \tag{14}$$

where, $d_{j,k}$ represents wavelet coefficients at different scales and positions, j is the scale index, k is the position index. The symbol "| |" represents the modulus value, the symbol "max( )" represents taking the maximum value, and the symbol "t[ ]" represents taking the corresponding time.

3.4 Traveling Wave Head Inversion Based on CNN

The steps of the entire method are shown in Fig. 8:

(1) Firstly, through wavelet transform, the amplitude characteristics of the traveling waves on the primary and secondary sides of the sensor are recorded as training samples, resulting in a total of k sets of samples.
(2) Train these k sets of samples using CNN to obtain the inverse transfer characteristics of the sensor.
(3) Based on the inverse transfer characteristics of the sensor mentioned above, the traveling waves on the secondary side of the sensor in the fault line are processed, and finally, the fault traveling waves on the primary side of the sensor at both ends of the line are reconstructed by inversion.
(4) Using the double-ended traveling waves obtained from the above inversion, the times t_M and t_N for the traveling waves to reach both ends of the line are obtained by identifying the wave head.
(5) Based on the double-ended traveling wave method, the fault location is achieved by Eq. (13).

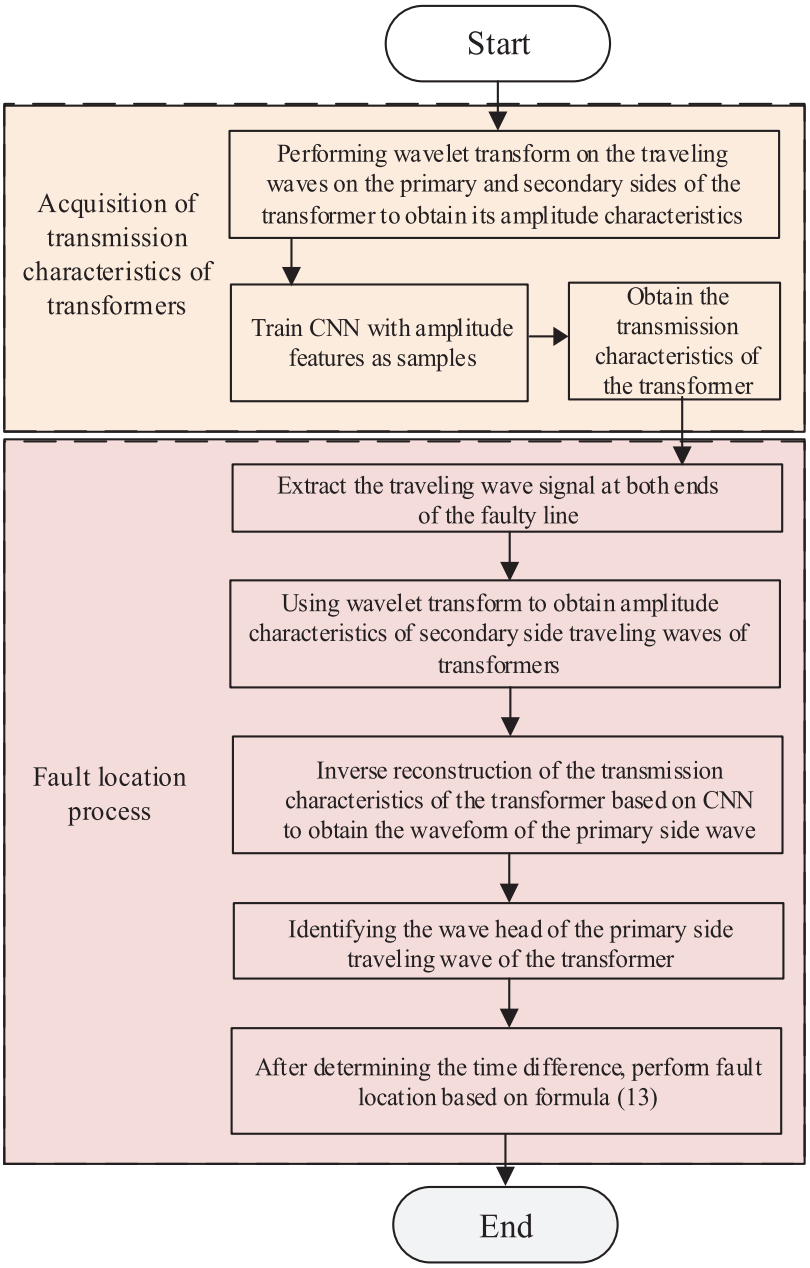

Figure 8: Operational flow chart

4 Simulation Verification

4.1 Simulation Model

Using grounding faults in wind farm distribution lines as the validation scenario for this method. As shown in Fig. 9, a simulation experimental model of the wind farm line was built in PSCAD/EMTDC. The wind farm adopts permanent magnet direct drive motors, and the machine side inverter adopts maximum power tracking control. The output voltage of the unit is transmitted to the medium voltage bus through cables, and then transmitted to the AC power grid by overhead lines. The monitoring points are set at the beginning and the end of the line and at the connection between the overhead line and the cable.

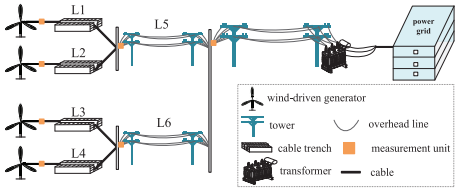

Figure 9: Topology of wind farm collector system

Both cable lines and overhead lines use frequency-dependent models, with a simulation sampling frequency set at 1 MHz and a model solving time step of 1 μs. The structural parameters of overhead lines and cables are shown in Tables 2 and 3, the relevant parameters of CVT simulation components are shown in Table 4. The lengths of the four cable lines are 10, 9.6, 8, and 8.8 km, respectively, with the cable shields grounded at both ends. The length of both overhead lines is 10 km. The wave velocity in the cable is taken as 150 m/μs, and the wave velocity in the overhead line is taken as 296 m/μs. The effectiveness of the method is analyzed at different fault distances, fault resistances, and fault initial phase angles conditions.

Table 2: Overhead line configuration parameters

Parameter	Numerical value
shunt conductance (S/m)	1×10^{-11}
Outer radius of wire (m)	0.0203454
Direct current resistance of wire (Ω/km)	0.03206
Relative magnetic permeability of wire	1.0
Outer radius of grounding wire (m)	0.0055245
Grounding wire DC resistance (Ω/km)	2.8645
Relative magnetic permeability of grounding wire	1.0

Table 3: Cable configuration parameters

Parameter	Numerical value
Outer radius of wire core (m)	0.0132
Core resistivity (Ω·m)	1.724e−8
Relative magnetic permeability of wire core	1.0
Inner radius of insulation layer (m)	0.0132
Outer radius of insulation layer (m)	0.04225
Relative dielectric constant of insulation layer	2.3
Relative magnetic permeability of insulation layer	1.0
Inner radius of shielding layer (m)	0.04225
Outer radius of shielding layer (m)	0.0515
Shielding layer resistivity (Ω·m)	2.17e−7
Relative magnetic permeability of shielding layer	1.0

Table 4: Data partitioning scheme

Data set	Number of samples	Proportion
Training set	700	70.59%
Validation set	300	29.41%
Total	1000	100%

4.2 Fault Location Based on Correction of Wave Head Arrival Time

4.2.1 Data Generation and Preprocessing

The experimental data were generated using the model shown in Fig. 9 by PSCAD, with a total simulation time of 0.6 s (corresponding to 60,000 data points). The fault was simulated at 0.2 s after the start of the simulation (i.e., at the 20,000th data point), and the voltage signals at the beginning and end of the line during operation were recorded as raw data.

In order to ensure that the final generated training data has sufficient diversity and improves the robustness of the model to complex and variable faults, key fault parameters are systematically adjusted in the simulation settings of each fault type to simulate the changes in actual working conditions. This mainly includes:

(1) Fault distance: By dynamically changing the position of the fault point, the model can learn and identify the changes in signal propagation attenuation and traveling wave characteristics when a fault occurs in different locations.
(2) Fault resistance: By setting a range of different resistance values from zero ohms to several hundred ohms, which reflects the different fault resistance conditions that may occur during the fault process.
(3) Fault initial phase angle: By generating faults at different starting times of the power supply voltage from 30° to 90°, the initial traveling wave characteristics at different fault initial phase angles are captured.

Taking into account the various factors mentioned above, a large number of combined simulation experiments were conducted to generate 1000 sets of effective raw fault data that can reflect different fault conditions.

To improve the effectiveness of characteristic data, reduce the computational complexity of the model, and accelerate convergence, preprocessing is performed on the original voltage signal. The steps are as follows:

(1) Signal clipping: Extract representative time periods centered around the fault point, specifically 665 data points before the fault occurs and 2335 data points after the fault occurs. This window can fully capture the transient characteristics of the fault.
(2) Feature extraction: The clipped signal is subjected to a wavelet transform using the db6 wavelet basis function, and the amplitude of the high-frequency coefficients in the first layer is selected as the key vector representing the high-frequency features of the traveling wave.
(3) Data standardization: To eliminate dimensional differences between feature vectors, unify feature scales, and accelerate neural network convergence, the extracted high-frequency amplitude feature vectors are normalized. Using the minimum maximum normalization method, map the eigenvalues to the [0, 1] interval, with the following Eq. (15):

$$x_{nor} = \frac{(x - x_{\min})}{(x_{\max} - x_{\min})} \tag{15}$$

where x is the original feature value, x_{min} and x_{max} are the minimum and maximum values of the feature dimension on the entire training set, respectively.

After preprocessing, the 1000 sets of sample data were divided into training and validation sets by category, as shown in Table 4, to ensure that the training and validation processes can evaluate model performance on balanced and independent data.

4.2.2 Parameter Settings of CNN

CNN is selected as the core model to learn the nonlinear mapping relationship between the secondary side and the primary side of the sensor. Subsequently, after multiple iterations of training, the architecture and hyperparameters of the network were determined, and the selected hyperparameters are shown in Table 5.

Table 5: CNN hyperparameters

Hyper-parameters	Numerical value
Initial learning rate	0.001
Maximum number of iterations	100
Learning rate decline cycle	50
Learning rate decline factor	0.1

After the completion of network debugging and training, the root mean square error (RMSE) and loss value of the training process vary with iteration rounds, as shown in Fig. 10.

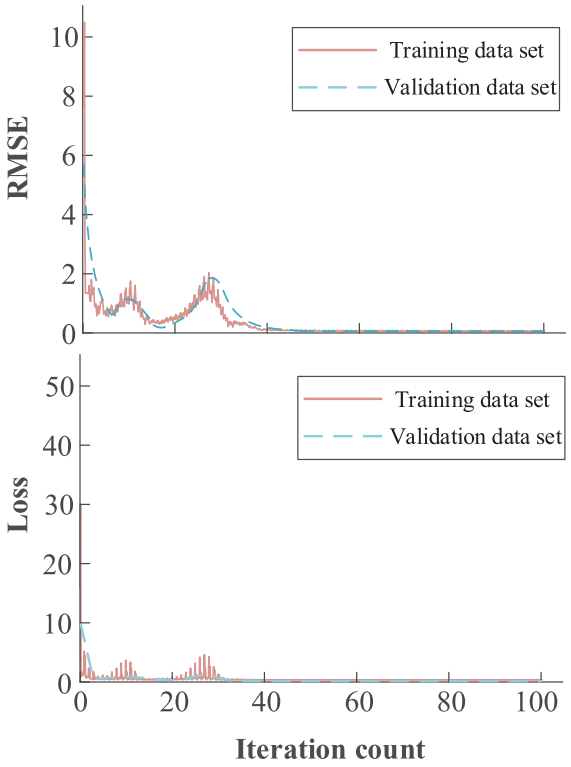

Figure 10: Training and validation loss with RMSE vs. iteration number

According to the analysis of Fig. 10, the model shows a good convergence trend within the set of 100 training cycles. The training loss and RMSE value decrease rapidly in the first 50 rounds, and when the learning rate decreases according to the preset strategy in the 50th round, the rate of decrease slows down and eventually stabilizes. This indicates that the model effectively learned the intrinsic patterns of the data in the training set and achieved a relatively ideal convergence state.

4.2.3 Inversion of Traveling Waves on the Primary Side

Preprocess the zero-mode voltage signals collected from the secondary side of the sensor at the beginning and end of the line during faults to obtain standardized eigenvectors that are completely consistent with the sample data. Input this feature vector into the trained convolutional neural network, and the network output is the reconstructed primary side zero sequence voltage feature signal. Fig. 11a,b shows the comparison of characteristics between the first layer of the primary and secondary signals at the beginning and end of the line and the first layer characteristics of the inverted signal, respectively.

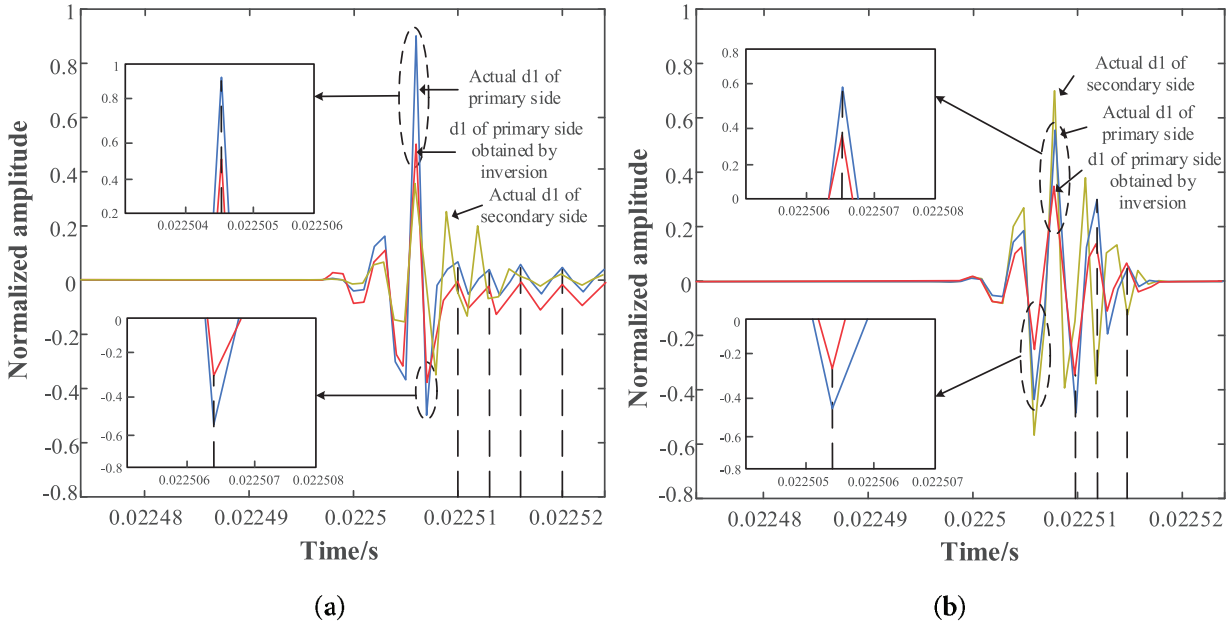

Figure 11: Comparison of actual primary and secondary side *d*1 and the *d*1 coefficient obtained by inversion at different ends: (**a**) *d*1 coefficient waveforms of the beginning monitoring point, (**b**) *d*1 coefficient waveforms of the end monitoring point

From Fig. 11, it can be seen that the *d*1 detail coefficients of the primary side obtained by the inversion model exhibit extremely high consistency with the actual signal of the primary side, whether in terms of overall waveform shape, amplitude variation, or key details. Especially in the locally amplified regions (such as around 0.02249 and 0.02250 s), the peak values and estimated moments of the inverted signal are almost identical to those of the actual primary side signal, indicating that the CNN inversion results accurately capture the dynamic characteristics of the actual primary side *d*1 layer detail coefficients. Therefore, compared to directly using the secondary side *d*1 layer detail coefficients, the inverted primary side *d*1 layer detail coefficients have high fidelity to the actual primary side, providing a more reliable basis for calibrating the wave head and improving the accuracy of subsequent traveling wave location.

4.2.4 Fault Location Method

Set a fault on line L1, with the fault distance set at 5 km from the beginning of the line, denoted as x_a. The fault resistance R_f is 100 Ω, and the initial phase angle of the fault θ_f is 45°. Perform wavelet decomposition on the secondary voltage measured by the sensor to extract high-frequency amplitude characteristic components. By using the inverse wavelet features, the time calibration for the traveling wave to reach both ends of the line is achieved, as shown in Fig. 12, which displays the time difference for the traveling wave to reach both ends of the line.

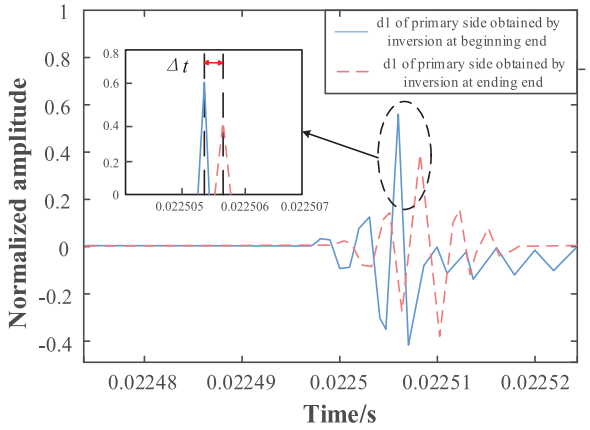

Figure 12: Corrected time difference of traveling wave head arrival

Substitute the corrected wave head time into Eq. (13) to calculate the fault distance, x_c = 5.15 km.

This paper uses the relative error rate to characterize the accuracy of fault location. The definition of relative error in fault distance measurement is as follows:

$$e = \frac{|x_c - x_a|}{l} \times 100\% \tag{16}$$

where x_c is the calculated fault distance, and l is the length of the fault line. The relative distance measurement error in this case is e = 1.5%.

4.3 Adaptive Analysis

4.3.1 The Influence of Fault Distance and Fault Transition Resistance

Fig. 13 shows the fault location errors when the initial phase angle of the fault is 45°, and the fault distances are 1, 3, 5, 7, and 9 km, respectively, and the fault transition resistance value is 0, 50, 100, 150, and 200 Ω, respectively.

From the data in Fig. 13, it can be seen that the relative error is less affected by the fault distance, due to the limited length of each section of the distribution line. However, as the fault resistance increases, the relative error rate shows an increasing trend. When the fault resistance is less than 100 Ω, the error corresponding to all fault distances remains at a low level, with the highest being 5% and the lowest being only 0.25%, and the curve trend is relatively smooth. This indicates that under low fault resistance conditions, the method proposed in this paper has high accuracy. When the fault resistance is greater than 100 Ω, the relative error rate shows an upward trend, which is due to the intensified attenuation of the traveling wave signal in high resistance fault scenarios, leading to an increase in the error rate of wave head detection. However, the

relative error rate can still be controlled within 5%, indicating that the proposed method can still maintain good location accuracy at higher fault transition resistance.

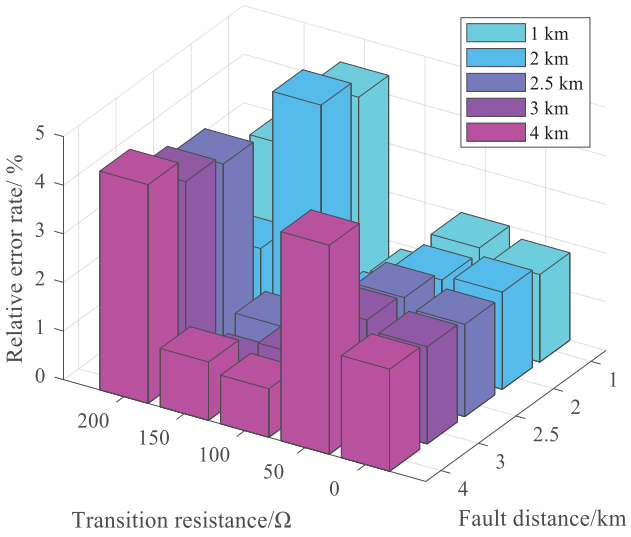

Figure 13: Average error rate of the proposed method under different fault distances and fault resistances

4.3.2 The Influence of Fault Initial Phase Angle

Set the fault distance to 3 km, the fault resistances are 0, 100, and 200 Ω, respectively, and the initial phase angles of the fault are set to 30°, 60°, and 90°, respectively. As shown in Fig. 14, it can be known that under different fault initial phase angle conditions, the relative error rate of distance measurement corresponding to each fault resistor is generally at a low level, and even under different initial phase angles of faults, the relative error rate of distance location also remains below 5%.

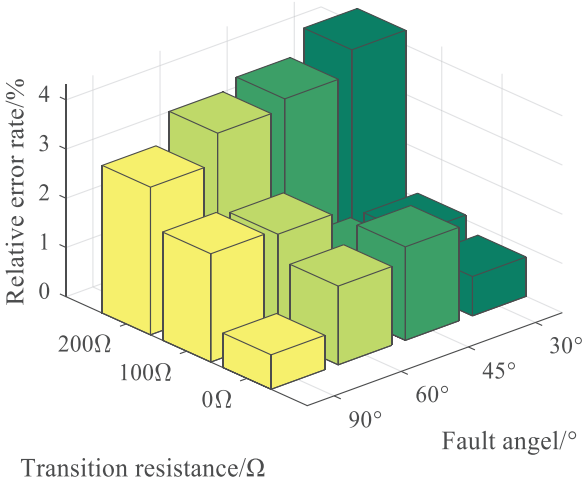

Figure 14: Average error rate of the proposed method with different initial phase angle of fault

4.4 Comparison with Existing Methods

Apply the existing method of traveling wave location to compare with the method proposed in this paper. The comparison results are shown in Table 6.

Table 6: Comparison with existing methods

Method	Applicable scenarios	Supported sensors types	Inversion method	Sampling rate	Location error
[11]	Transmission grid	CVT	Frequency division inversion	1 MHz	2.5%
[13]	Transmission grid	Rogowski coil	Circuit model inversion	1 MHz	1.2%
[15]	Transmission grid	Rogowski coil	No inversion	250 kHz	5.8%
[20]	Transmission and distribution grid	CVT	Inversion of full waveform	1 MHz	4.7%
[30]	Transmission grid	Rogowski coil	No inversion	10 MHz	2.9%
Proposed method	Transmission and distribution networks	All types	Inversion after wavelet transform	1 MHz	2.2%

Table 6 compares the performance indicators of the method proposed in this paper with several related methods. From the perspective of the implementation of wave head identification, the methods in references [15,30] did not use waveform inversion, while the methods in references [11,13,20], and this paper all utilize the principle of waveform inversion. The accuracy of the former is much lower than that of the latter, indicating that wave head inversion plays a significant role in improving the accuracy of fault localization. Among several positioning methods that utilize inversion principles, reference [13] has the highest accuracy, but its applicability is for fault traveling wave positioning applications in traditional transmission lines whose sensor can only be used for traditional Rogowski coil and cannot meet the fault location requirements of mixed line scenarios in distribution networks. Reference [11] has slightly lower accuracy than the method proposed in this paper, but it cannot be applied to distribution networks. Although the method proposed in reference [20] can be applied to distribution networks and is specific to CVTs, its accuracy is significantly lower than that of the method proposed in this paper. In addition, from the perspective of the sampling frequency required by the method, although the sampling frequency of the method in reference [15] is the lowest, its positioning accuracy is also poor. Under the condition of using a frequency of 1 MHz, the method proposed in this paper not only ensures high positioning accuracy, but also ensures its comprehensive performance for mixed lines in distribution networks and multiple types of sensors.

5 Conclusion

This paper focuses on the problem of fault location using traveling waves in distribution lines. A fault location method based on primary travelling wave head inversion is proposed. The main conclusions are as follows:

(1) Compared to using the secondary side traveling wave signal of the sensor directly, using CNN to invert and reconstruct the traveling wave head of the primary side of the sensor through the signal from the secondary side, which can reduce the sensing distortion of the sensor on the traveling wave waveform, thereby improving the location accuracy. This method is particularly suitable for other types of unconventional traveling wave sensors besides conventional Roche coil current sensors.

(2) By fully considering the influence of fault distance, fault transition resistance, and fault initial phase angle, a black box model of sensor transmission characteristics can be constructed using neural networks to ensure the universality of the model with different fault conditions.

(3) Under various fault conditions, the location accuracy of the proposed method remains at a high level, and its maximum average location error does not exceed 2.2%, demonstrating the robustness and effectiveness in different scenarios.

(4) The construction of the training sample set is an important factor affecting the accurate acquisition of the inverse transfer characteristics of sensors. In practical applications, this method requires the generation of various primary side traveling wave head signals to construct training samples, and manual simulation methods require a large amount of work. In the future, the development of an automatic traveling wave head generation device will be considered to further improve the efficiency of this method.

Acknowledgement: Not applicable.

Funding Statement: This work is funded by the Science and Technology Project of State Grid Corporation of China (grant No.: 5500-202318538A-3-2-ZN).

Author Contributions: Guanghua He: Writing—review & editing, Funding acquisition, Project administration. Jinlong Qi: Writing—review & editing, Conceptualization, Methodology. Yao Feng: Writing—original draft, Formal analysis, Methodology, Validation. Jiayi Han: Writing—review & editing. Heng Chen: Methodology, Writing—review & editing. Baoming Huang: Visualization, Software. Jiangtao Li: Investigation, Validation. All authors reviewed the results and approved the final version of the manuscript.

Availability of Data and Materials: The data used to support the findings of this study are included within the article.

Ethics Approval: Not applicable.

Conflicts of Interest: The authors declare no conflicts of interest to report regarding the present study.

References

1. Wang D, Yu D, Gao H, Peng F, Lin J, Wang J, et al. Frequency modification algorithm-based traveling wave fault location approach for overhead transmission lines with structural changes. Prot Control Mod Power Syst. 2025;10(2):1–12. doi:10.23919/PCMP.2024.000007.
2. Zeng X, Tong X, Tong N. A novel protection relay for neutral effectively grounded distribution networks independent on sequence components. Int J Electr Power Energy Syst. 2024;159:110036. doi:10.1016/j.ijepes.2024.110036.
3. Leng H, He S, Qiu J, Liu F, Huang X, Zhu J. Multi-branch fault line location method based on time difference matrix fitting. Energy Eng. 2024;121(1):77–94. doi:10.32604/ee.2023.028340.
4. Shu H, Duan D, Tian X. Single-ended fault location for direct distribution overhead feeders based on characteristic distribution of traveling waves along the line. Electr Power Syst Res. 2020;185:106345. doi:10.1016/j.epsr.2020.106345.
5. Dong XZ, Chen BS, Dong QH, Dai YY. Traveling waves fault location of distribution lines based on distributed voltage sensing technology. Power Syst Technol. 2023;47(12):4837–47. (In Chinese). doi:10.13335/j.1000-3673.pst.2023.1576.
6. Deng F, Zeng X, Pan L. Research on multi-terminal traveling wave fault location method in complicated networks based on cloud computing platform. Prot Control Mod Power Syst. 2017;2:19. doi:10.1186/s41601-017-0042-4.
7. Zhang C, Song G, Wang T, Wu L, Yang L. Non-unit traveling wave protection of HVDC grids using levenberg–marquart optimal approximation. IEEE Trans Power Deliv. 2020;35(5):2260–71. doi:10.1109/tpwrd.2020.2964717.
8. Wang D, Jin W, Zhang J, Gao Y, Hou M. Travelling wave fault location algorithm for hybrid cable-overhead transmission lines based on frequency-dependent characteristic. Int J Electr Power Energy Syst. 2025;171:111042. doi:10.1016/j.ijepes.2025.111042.

9. Abd el-Ghany HA, Soliman IA, Azmy AM, Nahas EW. Robust fault line identification and precise localization in wide-area networks using traveling wave techniques. Electr Power Syst Res. 2026;253:112494. doi:10.1016/j.epsr.2025.112494.
10. Zeng J, Zeng X, Bai H, Yu K, Xu M, She X, et al. A novel fault location method for multi-terminal transmission lines based on composite analysis of time-frequency fault traveling waves. Int J Electr Power Energy Syst. 2025;167:110600. doi:10.1016/j.ijepes.2025.110600.
11. Tang T, Li X, Zeng X, Zhou Y, Yuan K, Bi L. Accurate detection method of traveling wave shape based on EEMD and L1 norm regularization. Int J Electr Power Energy Syst. 2024;159:110008. doi:10.1016/j.ijepes.2024.110008.
12. Zhang M, Wang D, Gao H, Peng F, Gao M. Novel traveling wave fault location method for HVDC transmission line based on wavefront frequency. Electr Power Syst Res. 2024;234:110598. doi:10.1016/j.epsr.2024.110598.
13. Xia Y, Li Z, Wang S, Sun J, Guo X. Traveling wave inversion method of power line faults. Int J Electr Power Energy Syst. 2023;149:109025. doi:10.1016/j.ijepes.2023.109025.
14. Hu MF, Liu Y, Hua B. Distributed fault location for distribution networks under optimal configuration of measuring devices. Power Syst Technol. 2021;45(7):2616–22. (In Chinese). doi:10.13335/j.1000-3673.pst.2020.1210.
15. Li Z, Lin R, Wang J, Zheng W. Adaptive-fuzzy-neural-network data-fusion-based fault-location technique using wide-area synchronized measurements for transmission grids. In: 2020 5th Asia Conference on Power and Electrical Engineering (ACPEE); 2020 Jun 4–7; Chengdu, China. p. 105–11. doi:10.1109/acpee48638.2020.9136541.
16. AsghariGovar S, Seyedi H. A novel transfer matrix-based approach for pilot protection of hybrid transmission lines considering HIF location. IEEE Trans Power Deliv. 2020;35(4):1749–57. doi:10.1109/tpwrd.2019.2952538.
17. Gashteroodkhani OA, Majidi M, Etezadi-Amoli M, Nematollahi AF, Vahidi B. A hybrid SVM-TT transform-based method for fault location in hybrid transmission lines with underground cables. Electr Power Syst Res. 2019;170(1):205–14. doi:10.1016/j.epsr.2019.01.023.
18. Yu K, Bi L, Zeng X, Wu H, Ni Y. Induction fault traveling wave measurement technique based on tunnel magnetoresistance. IEEE Trans Power Deliv. 2023;38(6):4347–57. doi:10.1109/TPWRD.2023.3319141.
19. Xie W, Xue F, Chen X, Liu X, Li Z. CVT stray capacitance optimization based on multi-random variable parameter optimization method. In: Proceedings of the 2nd International Conference on Information Technologies and Electrical Engineering; 2019 Dec 6–7; Zhuzhou, China. doi:10.1145/3386415.3387021.
20. Li ZW, Du YD, Lin YQ, Zhao T, Xiao RP. A method of voltage wave accurate detection based on Tikhonov regularization theory. Power Syst Technol. 2019;43(3):1049–55. (In Chinese). doi:10.13335/j.1000-3673.pst.2018.0942.
21. Liu F, Wu YZ, Li XB, Cai TT, Chen JJ, Kuang Y, et al. Method for fault traveling wavefront calibration based on improved optical voltage transformer. J Electr Power Sci Technol. 2025;40(4):38–49. (In Chinese). doi:10.19781/j.issn.1673-9140.2025.04.004.
22. Li Z, Lv J, Xi Y, Xiong Y, He Z, Liu J. Accurate detection method of voltage traveling-wave-based on waveform inversion. Electr Power Syst Res. 2020;178:106033. doi:10.1016/j.epsr.2019.106033.
23. Dziuda L, Niewczas P, Fusiek G, McDonald JR. Hybrid fiber optic voltage sensor for remote monitoring of electrical submersible pump motors. Opt Eng. 2005;44(6):064401. doi:10.1117/1.1926947.
24. Wu HJ, Wu XY, Shen F, Sun SD, Hu YF. Fault location system based on wavelet analysis for power grid voltage traveling wave. Electron Des Eng. 2024;32(16):39–42,48. (In Chinese). doi:10.14022/j.issn1674-6236.2024.16.008.
25. Li XY, Deng F, Zhang Z, Jiang SX, Bi LX. High precision detection method for a voltage traveling wave based on L1 regularization inversion. Power Syst Prot Control. 2023;51(22):167–76. (In Chinese). doi:10.1016/j.ijepes.2024.110008.
26. Li Z, Yu C, Abu-Siada A, Li H, Li Z, Zhang T, et al. An online correction system for electronic voltage transformers. Int J Electr Power Energy Syst. 2021;126:106611. doi:10.1016/j.ijepes.2020.106611.
27. Kubo T, Furukawa T, Fukumoto H, Ohchi M. Numerical estimation of characteristics of voltage-current sensor of resin molded type for 22 kV power distribution systems. In: 2009 ICCAS-SICE; 2009 Aug 18–21; Fukuoka, Japan. p. 5050–4.
28. Gao C, Li W, Mao J, Hu S, Zhang B, Yang S. Non-intrusive cable fault diagnosis based on inductive directional coupling. IEEE Trans Power Deliv. 2019;34(4):1684–94. doi:10.1109/tpwrd.2019.2918173.

29. Zhuang C, Xie S, Yang H, Yu H, Geng Y, Zeng R. Flexible noncontact approach for fault location of transmission lines using electro-optic field sensors. IEEE Trans Electromagn Compat. 2021;63(6):2151–8. doi:10.1109/temc.2021.3108938.
30. Liu Y, Sheng G, He Z, Jiang X. A traveling wave fault location method for earth faults based on mode propagation time delays of multi-measuring points. Prz Elektrotech. 2012;88(3):254–8.
31. Ricki RS, Dicky DH, Apriyansyah B. Fast region-based convolutional neural network in object detection: a review. Int J Adv Comput Inform. 2025;2(1):34–40. doi:10.71129/ijaci.v2i1.pp34-40.
32. Erniwati S, Afifah V, Imran B. Mask region-based convolutional neural network in object detection: a review. Int J Adv Comput Inform. 2025;1(2):106–17. doi:10.71129/ijaci.v1i2.pp106-117.